



CAN UNCLASSIFIED

DRDC | RDDC  
technologysciencetechnologie



# The Empirical Canadian High Arctic Ionospheric Model (E-CHAIM)

## *Bottomside*

David, Themens

P.T. Jayachandran  
Anthony McCaffrey  
Benjamin Reid  
University of New Brunswick

Prepared by:  
University of New Brunswick  
8 Bailey Drive  
P.O. Box 4400  
Fredericton (New Brunswick) E3B 5A3  
Canada  
PSPC Contract Number: W7714-186507/001/SS  
Technical Authority: Thayananthan Thayaparan, Defence Scientist  
Contractor's date of publication: June 2018

**Defence Research and Development Canada**

**Contract Report**

DRDC-RDDC-2018-C184

October 2018

CAN UNCLASSIFIED

**IMPORTANT INFORMATIVE STATEMENTS**

This document was reviewed for Controlled Goods by Defence Research and Development Canada using the Schedule to the *Defence Production Act*.

Disclaimer: This document is not published by the Editorial Office of Defence Research and Development Canada, an agency of the Department of National Defence of Canada but is to be catalogued in the Canadian Defence Information System (CANDIS), the national repository for Defence S&T documents. Her Majesty the Queen in Right of Canada (Department of National Defence) makes no representations or warranties, expressed or implied, of any kind whatsoever, and assumes no liability for the accuracy, reliability, completeness, currency or usefulness of any information, product, process or material included in this document. Nothing in this document should be interpreted as an endorsement for the specific use of any tool, technique or process examined in it. Any reliance on, or use of, any information, product, process or material included in this document is at the sole risk of the person so using it or relying on it. Canada does not assume any liability in respect of any damages or losses arising out of or in connection with the use of, or reliance on, any information, product, process or material included in this document.

# **The Empirical Canadian High Arctic Ionospheric Model (E-CHAIM)**

*Bottomside*

David R. Themens  
University of New Brunswick

P.T. Jayachandran, Anthony M. McCaffrey, Benjamin Reid  
University of New Brunswick

Prepared For:  
Department of National Defence  
DRDC-Ottawa, BLDG 29, 3701 Carling Ave.  
Ottawa, Ontario, K1A0Z4, Canada  
Contract # W7714-186507/001/SS

The following work is supported through the All Domain Situational Awareness (ADSA) Science & Technology program, contract number W7714-186507/001/SS.

- © Her Majesty the Queen in Right of Canada, as represented by the Minister of National Defence, [2018]
- © Sa Majesté la Reine (en droit du Canada), telle que représentée par le ministre de la Défense nationale, [2018]

## Abstract

---

In this study, we present a bottomside model representation to be used by the Empirical Canadian High Arctic Ionospheric Model (E-CHAIM). This model features a new approach to modeling the bottomside electron density; namely, instead of modelling electron density directly, E-CHAIM models the altitude profile of the scale thickness of a single bottomside layer. In this approach the curvature in the bottomside associated with the E-region and F1-layer is represented in the scale thickness domain as a peak function centered at the layer peak altitude. The use of this approach ensures the production of explicitly doubly differentiable bottomside electron density profiles and directly avoids issues known to exist within current standard, such as the International Reference Ionosphere (IRI), which has discontinuities in space, time, and in the vertical electron density gradient. In terms of performance, after removing the impacts of hmF2 and NmF2, the new E-CHAIM profile function generally performs comparably to the IRI, with bottomside TEC within 1.6 TECU of observations. More specifically, the E-CHAIM bottomside is demonstrated to outperform the IRI bottomside function in the F-region during low solar activity periods. At high latitudes, E-CHAIM tends to outperform the IRI during winter months by between 10% and 40% of NmF2 while being outperformed by the IRI by between 10% and 25% of NmF2 during summer periods, particularly during the daytime at high solar activity.

## Significance for Defence and Security

---

This work is a direct extension of the previous E-CHAIM NmF2 and hmF2 model components to reflect the electron density of the ionosphere below the F2-peak. The development of this model component is a necessary extension of the F2-peak models required for the simulation of oblique incidence HF propagation. This study has demonstrated that there exist significant errors in current communications models with respect to the representation of the F1-layer height. Furthermore, this study demonstrates discontinuities in the horizontal electron density, in the vertical gradient of electron density, and in the diurnal and seasonal variation of electron density of current standards (the IRI). These issues can result in unstable behaviour in HF ray tracing and band forecasting applications. All of these issues are resolved in the new E-CHAIM model while not having to make any sacrifices with respect to performance.

## Résumé

---

Dans cet article, nous décrivons la représentation du modèle du « bas » utilisée par le *Modèle empirique de l'ionosphère du haut arctique canadien* (E-CHAIM). Ce modèle comporte une nouvelle méthode de modéliser la densité électronique au bas de l'ionosphère. E-CHAIM modélise le profil d'altitude de l'épaisseur de l'échelle d'une unique couche inférieure plutôt que de modéliser directement la densité d'électrons. Avec cette méthode, la courbure du bas associée à la région E et la région F<sub>1</sub> est représentée dans le domaine de l'épaisseur de l'échelle comme une fonction de maximum centrée à l'altitude maximale de la couche. Cette démarche assure la production de profils deux fois dérivables de la densité d'électrons au bas de la couche et évite directement les problèmes connus des modèles standards actuels, comme l'ionosphère internationale de référence (IIR), qui présente des discontinuités dans l'espace, le temps et le gradient vertical de densité d'électrons. Au chapitre du rendement, après avoir retiré les effets de la  $h_mF_2$  et de la  $N_mF_2$ , la nouvelle fonction de profil du modèle E-CHAIM se comporte de manière comparable à l'IIR, en prédisant une teneur totale en électrons (TEC) au bas, en deçà de 1,6 unité de TEC des valeurs observées. Plus particulièrement, nous avons montré que la fonction du fond du modèle E-CHAIM surpasse la fonction de fond de la région F pendant les périodes de faible activité solaire. Aux hautes latitudes, E-CHAIM tend à surpasser l'IIR pendant l'hiver par environ 10 % à 40 % pour la  $N_mF_2$  alors que l'IIR surpasse E-CHAIM par environ 10 à 25 % pour la  $N_mF_2$  pendant l'été, notamment durant le jour pendant les périodes de forte activité solaire.

## Table of contents

---

Abstract.....	i
Significance for Defence and Security .....	i
Résumé.....	ii
Importance pour la défense et la sécurité .....	ii
Table of contents .....	iii
List of figures .....	iv
List of tables .....	vi
Acknowledgements .....	vii
1 Introduction.....	1
2 Data .....	5
3 hmE and hmF1 .....	6
4 The E-CHAIM Bottomside Function .....	10
5 Parameterization of the Bottomside Scale Height Amplitudes.....	14
6 Validation .....	15
7 Comment Regarding Night Time Underestimation .....	21
8 Challenges due to Precipitation .....	23
9 Conclusion .....	25
References/Bibliography.....	26
List of symbols/abbreviations/acronyms/initialisms .....	29

## List of figures

---

Figure 1 Electron density from IRI2016 for 50°N at 150km altitude along a line of geographic longitude at 12:00 UTC (top) and the 24-hour diurnal variation at the same altitude and latitude for 50°E longitude (bottom). The red circles highlight discontinuous transitions between periods with and without an F1-Layer. ....	1
Figure 2 (Left) An example electron density profile at 50°N and 50°E at 10:00UTC generated using the IRI default options between 90km and 300km with a 0.5km step size. (Right) The height derivative of the vertical electron density profile illustrated on the left. The red circles highlight discontinuities in the electron density gradient. ....	2
Figure 3 Top: IRI Daily Bottomside Thickness Parameter (B0) from the Gulyaeva option (green), Table option (blue), and ABT-2009 option (black) at Millstone Hill at 00UTC. Ionosonde-derived values are plotted with purple diamonds. Bottom: Daily hmF2 from the IRI M(3000)F2-based model (green), Shubin model (blue), and AMTB-2013 model (black) at 00UTC. Ionosonde-derived hmF2 is plotted with purple diamonds. ....	3
Figure 4 Map of the stations used to fit the E-CHAIM bottomside model. The dashed line corresponds to the lower boundary of the model at 50°N geomagnetic latitude. The dotted line corresponds to 65°N geomagnetic latitude. ....	5
Figure 5 Plot of mean hmF1 behaviour vs. AACGM latitude (top left), AACGM local time (top right), integrated AE index (bottom left), and solar zenith angle (bottom right). Ionosonde measured values are represented by black squares, E-CHAIM is represented by connected black stars, NeQuick is represented by connected blue stars, the “traditional”/ICEPAC parameterization is represented by connected red stars, and a best fitted quadratic function in solar zenith angle is represented by connected green stars. ....	7
Figure 6 Example ionosonde-derived electron density profiles at Cambridge Bay (a-c) and corresponding scale height profiles (d-e) for three situations: (a,d) no E-region trace, (b,e) no F1-layer/ledge trace, and (c,f) a profile with all three layers present. (d-f) also demonstrate the various components of the scale height function, where the dotted line is the scale height function for the F1-layer/ledge, the dashed line is the constant term, the dash-dotted is the scale height function for the E-region, and the solid line is the final bottomside scale height function. ....	11
Figure 7 Contours of monthly median fitted $H_{F2}$ (top), $H_{F1}$ (middle), and $H_E$ (bottom) for the Dourbes ionosonde between 2006 and 2013. ....	13
Figure 8 F2-peak normalized monthly median electron density profiles at PFISR for various UT times between 2007 and 2015. Note that local time at Poker Flat is UT – 8.1 hours. ....	16
Figure 9 Model-to-measurement bottomside monthly median electron density errors for E-CHAIM (left) and the IRI (right) at PFISR between 2007 and 2015. ....	17



Figure 10 Differences between IRI and E-CHAIM bottomside electron density profile RMS errors at PFISR. Negative values correspond to periods and locations where E-CHAIM outperforms the IRI.....	18
Figure 11 Same as Figure 10 but for RISR (left) and the Svalbard ISR (right). .....	19
Figure 12 Bottomside electron content measured by the PFISR (left) and Svalbard (right) ISRs and that modeled by the IRI (red) and E-CHAIM (blue) between 2007 and 2015 at various UT times. Note that the Poker Flat local time is UT – 8.1 and that for Svalbard is UT + 1.4.....	20
Figure 13 Left: A manually scaled ionogram from the Millstone Hill Digisonde at 00:15 UT on January 29 <sup>th</sup> , 2010. Right: Corresponding vertical electron density profiles from the Millstone Hill ISR (solid black), the Millstone Hill ionosonde (dotted black), E-CHAIM anchored at the ionosonde hmF2 and NmF2 (dashed blue), and the IRI anchored at the ionosonde hmF2 and NmF2 (red dashed) at 00:15 UT on January 29 <sup>th</sup> , 2010 .....	21
Figure 14 Example electron density profiles from PFISR without (top) and with (bottom) auroral precipitation structures. Solid lines correspond to measured profiles, dotted lines correspond to E-CHAIM, and dashed lines correspond to the IRI. Note that ISR hmF2 and NmF2 have been used here in place of the model values to facilitate comparison of just the profile shape. Profile dates (day, month, year UTC) are provided in the title of each subplot.....	23

**List of tables**

---

Table 1 RMS errors from each hmF1 modeling method tested..... 8

## Acknowledgements

---

Infrastructure funding for CHAIN was provided by the Canadian Foundation for Innovation and the New Brunswick Innovation Foundation. Science funding is provided by the Natural Sciences and Engineering Research Council of Canada. The authors would like to thank the many ionosonde operators who provided data to this project. This paper uses ionospheric data from the USAF NEXION Digisonde network, the NEXION Program Manager is Mark Leahy. This publication makes use of data from the Qaanaaq and Nord ionosondes, owned by the U.S. Air Force Research Laboratory Space Vehicles Directorate and supported in part by the Air Force Office of Scientific Research. The authors thank Svend Erik Ascanius of the Danish Meteorological Institute and Denmark's Arctic Command for the operation of these ionosondes. This paper uses data from the Juliusruh Ionosonde which is owned by the Leibniz Institute of Atmospheric Physics Kuehlungsborn. The responsible Operations Manager is Jens Mielich. The authors are grateful to Konstantin Ratovski for the operation of the Irkutsk ionosonde. The Tromsø ionosonde is funded in part by QinetiQ.



# 1 Introduction

The Empirical Canadian High Arctic Ionospheric Model (E-CHAIM) project involves the development of a regional, fully three-dimensional, electron density model for use at high latitudes. The F2 peak of the model was first presented in Themens et al. [2017], while the topside portion of the model was presented in Themens et al. [2018]. We shall present and test the E-CHAIM bottomside parameterization in this study.

In terms of empirical bottomside models, there currently exist the successful parameterizations of the International Reference Ionosphere (IRI) [Bilitza, 1990; 2003; Reinisch and Huang, 2000] and NeQuick [Nava et al., 2008] models. While these models are widely used and have had demonstrated success at low and mid latitudes, we have nonetheless chosen to develop a separate bottomside of our own for E-CHAIM. This stems from some minor inadequacies that we have observed in these models. We summarize these concerns as follows:

- 1) The IRI uses an occurrence model of the F1-Layer. This often results in a sudden, discontinuous transition between periods with and without an F1-Layer. This is illustrated in Figure 1, where we see discontinuous jumps in the electron density in longitude and diurnally that are associated with the appearance of the F1-Layer in the model.

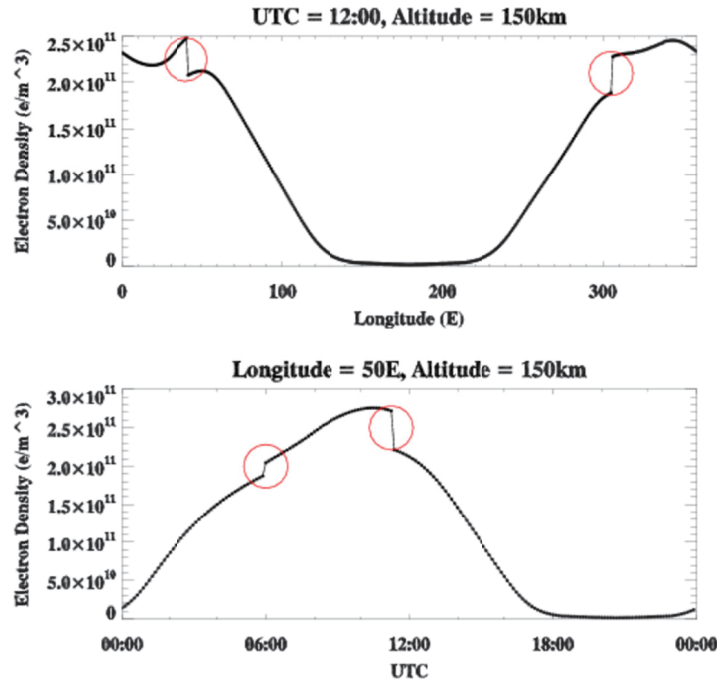


**Figure 1** Electron density from IRI2016 for 50°N at 150km altitude along a line of geographic longitude at 12:00 UTC (top) and the 24-hour diurnal variation at the same altitude and latitude for 50°E longitude (bottom). The red circles highlight discontinuous transitions between periods with and without an F1-Layer.

- 2) While the IRI's vertical transition between layers is piece-wise continuous, its derivatives are not continuous, as illustrated in Reinisch and Huang [2000] and here in Figure 2. These discontinuities in the derivative of the vertical electron density profile pose a challenge for HF ray tracing, which requires continuous derivatives [Kelso, 1968].

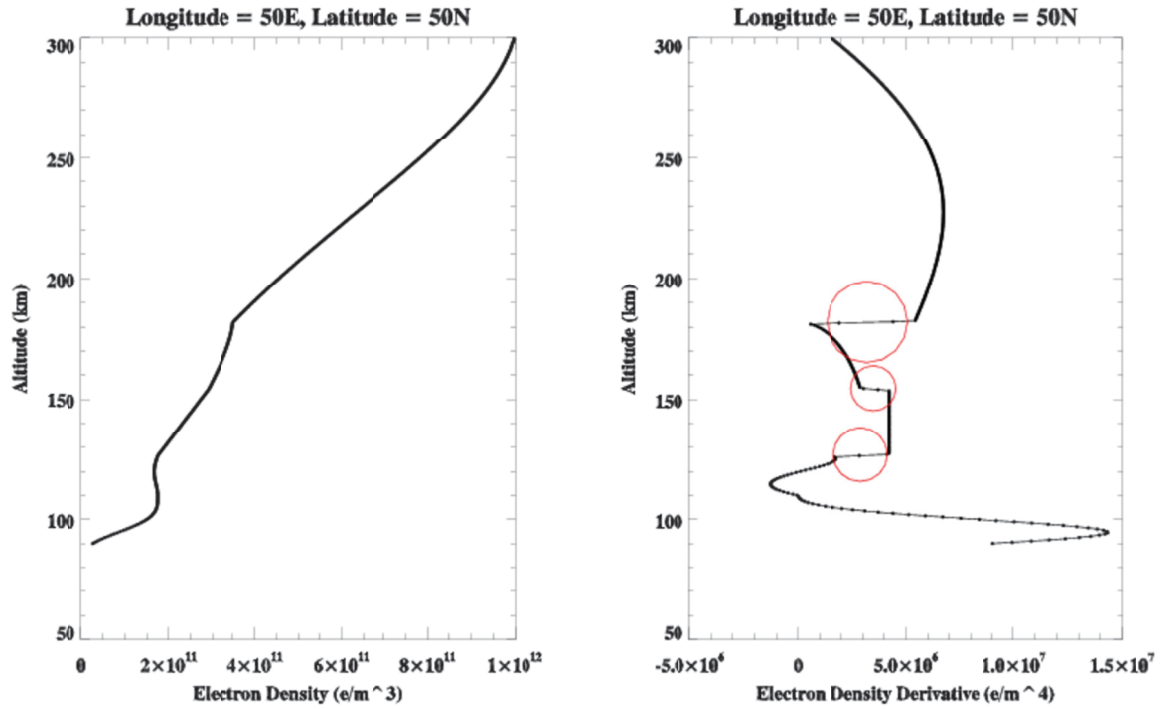


**Figure 2** (Left) An example electron density profile at 50°N and 50°E at 10:00UTC generated using the IRI default options between 90km and 300km with a 0.5km step size. (Right) The height derivative of the vertical electron density profile illustrated on the left. The red circles highlight discontinuities in the electron density gradient.

- 3) The F-region bottomside thickness (B0) parameterizations of the IRI include discontinuities in their seasonal variability. The ABT-2009 B0 option [Altadill et al., 2009], in particular, has a seasonal wrapping issue, where the end of one year does not match that of the next. These discontinuities in season for 00 UTC at Millstone Hill (42.6°N, 288.5°E) are illustrated in Figure 3.

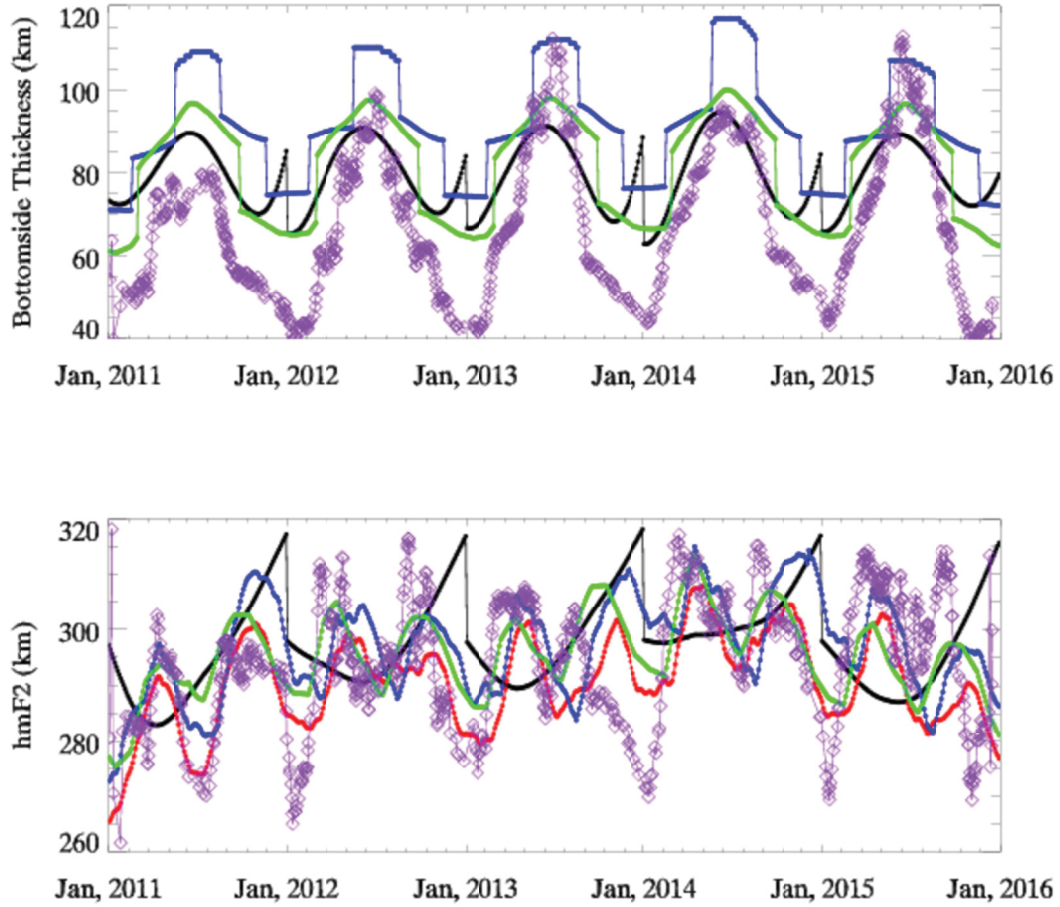


**Figure 3** Top: IRI Daily Bottomside Thickness Parameter ( $B0$ ) from the Gulyaeva option (green), Table option (blue), and ABT-2009 option (black) at Millstone Hill at 00UTC. Ionosonde-derived values are plotted with purple diamonds. Bottom: Daily  $hmF2$  from the IRI  $M(3000)F2$ -based model (green), Shubin model (blue), and AMTB-2013 model (black) at 00UTC. Ionosonde-derived  $hmF2$  is plotted with purple diamonds.

Note the anomalous enhancement in  $B0$  using the ABT-2009 option during the winter that is terminated at the year transition. As the ABT-2009 option was only fitted with data below  $60^\circ\text{N}$  geomagnetic latitude, this issue tends to be exacerbated as one tends to higher latitudes. A similar issue occurs for the AMTB-2013  $hmF2$  model (also illustrated in Figure 3), which uses the same methodology as the ABT-2009  $B0$  model. In Figure 3 the AMTB-2013  $hmF2$  model is a clear outlier; where all three other models and the ionosonde observations exhibit similar variability, characterized by a strong semi-annual variation, the AMTB-2013 model stands out by failing to represent this semi-annual variation and exhibiting discontinuous behaviour at the transition between years. These issues are now being examined by the IRI Working Group and should not require significant modifications to resolve; however, based on this the author would recommend the use of the Shubin  $hmF2$  model until such time as a fix is released for the AMTB-2013  $hmF2$  model.

- 4) The NeQuick's bottomside model is explicitly continuous in both electron density and its first derivative but, like the IRI, it uses a trigger for F1-Layer occurrence, which is based on foE in this case. This can, similarly, result in zonal and meridional discontinuities in the electron density between regions with and without an F1-Layer. For the E-region, the NeQuick mitigates a similar issue through the use of an exponential transition function, but no such mitigation is applied to the F1-Layer [Nava et al., 2008].

While these models are capable of capturing a wide range of bottomside shapes with their respective parameterizations, the above limitations push us to develop a new parameterization that avoids these issues. We have thus used the challenges and successes of the aforementioned bottomside formulations to inform our choice of bottomside model for E-CHAIM. In this way we have come to a formulation that, we believe, is robust and avoids the limitations of the above two models.

In Section 2, we discuss the data set used in the fitting of the E-CHAIM bottomside model. In Section 3, we discuss the parameterizations used for hmE and hmF1 in E-CHAIM, while Section 4 discusses the bottomside function itself and Section 5 discusses the parameterization of the various parameters used to define the E-CHAIM bottomside profile shape. Section 6 provides a brief validation of the E-CHAIM model and a comparison to the IRI. Finally, Section 7 proposes an explanation for errors common between the models, while Section 8 briefly discusses the challenges faced by such models during periods of strong precipitation.



## 2 Data

For the bottomside portion of the E-CHAIM model, we make use of ionosonde profiles from the Global Ionospheric Radio Observatory (GIRO) [Reinisch and Galkin, 2011] and the Canadian High Arctic Ionospheric Network (CHAIN) [Jayachandran et al., 2009]. We are here restricted to a substantially smaller dataset than what was available for the NmF2 and hmF2 portions of the model, as many of the older datasets did not invert electron density profiles from their data, instead scaling only foF2, MUF(3000)F2, and foE. In addition to this, the bottomside electron density profile, as a whole, is quite sensitive to scaling errors; thus, in addition to the quality control measures used for the hmF2 portion of the model (see Themens et al., [2017]) we have further restricted the dataset to data that has an Automatic Real-Time Ionogram Scaler with True height (ARTIST) quality control score of 90 or greater and to data that has been manually scaled. This quality control has resulted in a dataset of just over 6.2 million profiles. The stations used in constructing this dataset are represented in Figure 4.

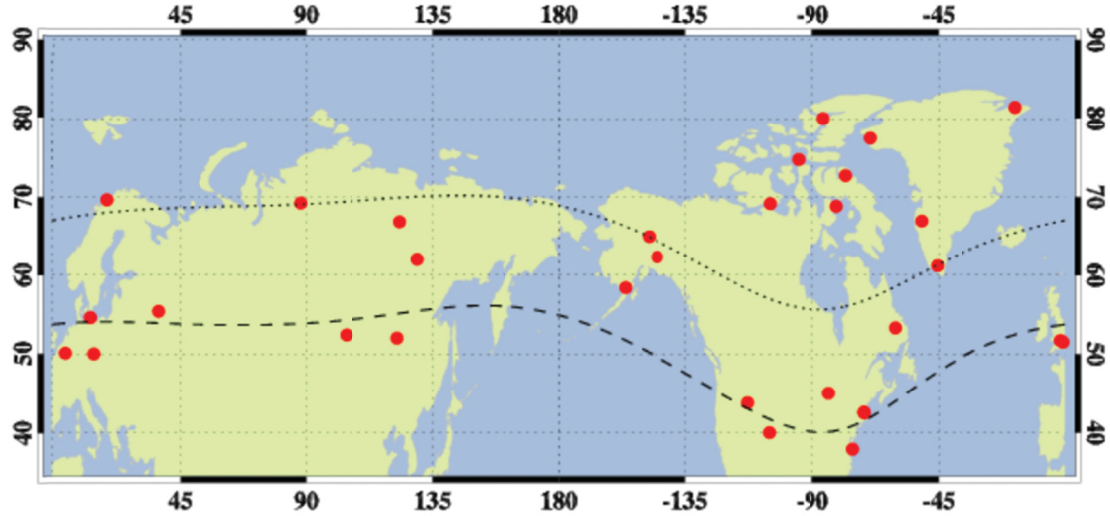


**Figure 4** Map of the stations used to fit the E-CHAIM bottomside model. The dashed line corresponds to the lower boundary of the model at 50°N geomagnetic latitude. The dotted line corresponds to 65°N geomagnetic latitude.

As one will note, the dataset has significant holes, particularly over central Canada and over the Arctic Ocean. To deal with this issue, the bottomside portion of our model is constructed in a magnetic latitude and magnetic local time coordinate system. In this way, we essentially “fill in” these data gaps by allowing each station to constrain the model along a zonal line at its magnetic latitude. Using such a coordinate system reduces the model’s capability to reproduce geographically-dependent structures, such as non-migrating tides, but this is an unfortunate necessary compromise, which has been used in the past for the IRI’s current default hmF2 and F2-layer bottomside thickness B0 models [Altadill et al., 2009; 2013].

### 3 hmE and hmF1

---

For the purpose of the E-CHAIM bottomside, we have chosen to independently develop models for hmE and hmF1. Beginning with hmE, we attempted to fit our dataset of ionosonde-derived hmE values to a model similar to that done for E-CHAIM’s topside thickness [Themens et al., 2018]. In so doing, we found RMS fitting errors hardly 0.5 km improved over the standard deviation of the input data. This implies that even sophisticated modeling approaches would only amount to a marginal improvement over simply using the average of the input data ( $102.19 \pm 5.02$  km). Based on this result, we have decided to use this average value in place of an explicit model for hmE. It is interesting here to note that both the IRI and NeQuick use constant values for hmE in their model; however, while the IRI’s value of 105 km falls within the error range of the average derived here, the NeQuick’s value of 120 km is substantially higher than the average by several standard deviations. This result may suggest a need to re-visit the NeQuick’s choice of hmE or could result from a strong latitudinal hmE dependence below the E-CHAIM domain (e.g. below  $50^\circ\text{N}$  geomagnetic latitude).

Unlike hmE, hmF1 demonstrated notable coherent variability, such that a model could provide a substantial improvement over the mean of the input data ( $175.31 \pm 15.01\text{km}$ ). For hmF1, we have used a similar framework to that used for the topside thickness but with a simplified AE index component. The full parameterization is given as

$$hmF1 = G + \sum_{l=0}^L \sum_{m=0}^{\min(l,M)} F_1 \left[ A_{lm} \cos\left(\frac{\pi m}{12} MLT\right) + B_{lm} \sin\left(\frac{\pi m}{12} MLT\right) \right] P_{lm}(\eta) \#(1)$$

$$\eta = \cos\left(90 - \varphi \frac{\pi}{45}\right) \#(2)$$

$$C_{lm}, D_{lm} = \sum_{c=1}^3 \alpha_{lm}^c \cos\left(\frac{2\pi c \cdot DoY}{365.25}\right) + \beta_{lm}^c \sin\left(\frac{2\pi c \cdot DoY}{365.25}\right) \#(3)$$

$$\begin{aligned} G = & a_1 \cos(\chi) + a_2 \sin(\chi) + a_3 \chi + a_4 \chi^2 + a_5 \chi^3 \\ & + \sin(\chi) \cdot (a_6 \sin \theta + a_7 \cos \theta) + \cos(\chi) \cdot (a_8 \sin \theta + a_9 \cos \theta) + a_{10} \sin \theta + a_{11} \cos \theta \\ & + AE'(a_{12} \sin \varphi + a_{13} \cos \varphi) \#(4) \end{aligned}$$

where  $F_1$  is 81-day smoothed F10.7 flux,  $AE'$  is integrated AE index using the same methodology as explained in the Themens et al. [2018],  $DoY$  is the day of year,  $\theta$  is the dipole tilt angle,  $\chi$  is the solar zenith angle in degrees, and  $a_{1-13}$ ,  $\alpha_{lm}^c$ , and  $\beta_{lm}^c$  are fitting coefficients. In the above parameterization,  $L$  and  $M$  are each set as three and the seasonal Fourier expansion is expanded up to triennial terms.

To assess the behaviour of the E-CHAIM hmF1 model fit, we present a comparison between hmF1 derived from E-CHAIM, the NeQuick parameterization (using measured hmF2), and the “traditional” hmF1 parameterization [Bilitza, 1990], currently used by Ionospheric

Communications Enhanced Profile Analysis & Circuit prediction program (ICEPAC) [Stewart, 1988] and given by

$$hmF1 = 165.0 + 0.6428 \cdot \chi \#(5)$$

If the  $hmF1$  from Equation 5 is greater than 200km,  $hmF1$  is instead set to 200km. A comparison of the median behaviour of  $hmF1$  from these various models is presented in Figure 5. To illustrate the best possible representation that could be achieved based solely on solar zenith angle, we have also considered a best fit to a quadratic function in solar zenith angle, given by the following

$$hmF1 = 179.91 - 0.43804 \cdot \chi + 0.0056225 \cdot \chi^2 \#(6)$$

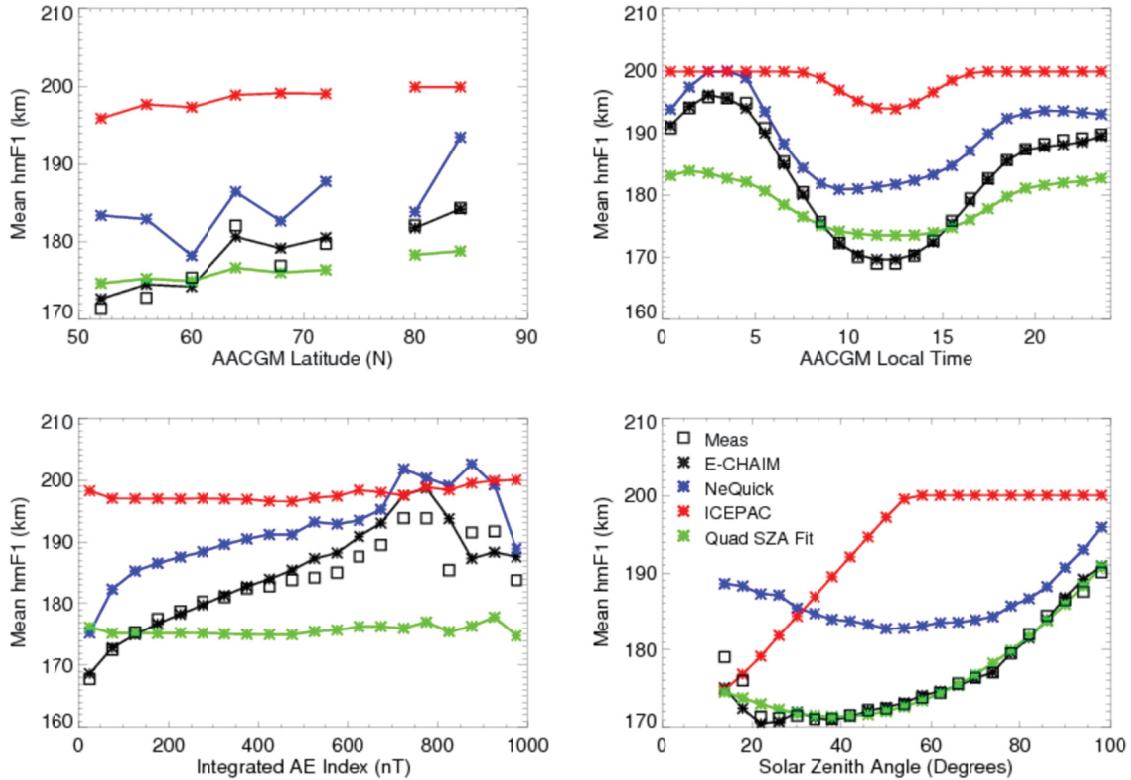


**Figure 5** Plot of mean  $hmF1$  behaviour vs. AACGM latitude (top left), AACGM local time (top right), integrated AE index (bottom left), and solar zenith angle (bottom right). Ionosonde measured values are represented by black squares, E-CHAIM is represented by connected black stars, NeQuick is represented by connected blue stars, the “traditional”/ICEPAC parameterization is represented by connected red stars, and a best fitted quadratic function in solar zenith angle is represented by connected green stars.

Examining first the patterns with respect to solar zenith angle, we see that the E-CHAIM and quadratic models fit the dataset’s solar zenith angle behaviour very well. Also evident is the apparent inability of a linear parameterization in solar zenith angle to represent the behaviour of  $hmF1$ , which appears to be largely unchanged except at large solar zenith angles. The NeQuick appears to perform well when the sun is low to the horizon but poorly during mid-day. In terms of

latitude, the ionosonde data demonstrates a largely linear trend, with hmF1 increasing toward the geomagnetic pole. This pattern is well captured by the E-CHAIM fit. The best fitted quadratic model seems to underestimate the rate of increase with latitude, while both the NeQuick and the “traditional” parameterization are biased upward by  $\sim 8$  km and  $\sim 30$  km, respectively. In local time, E-CHAIM and the ionosonde data demonstrate a minimum at local noon and an asymmetric diurnal variation with higher morning hmF1 compared to the evening. The existence of an F1 layer, even near local midnight, can be attributed to 24-hour sunlit conditions at high latitudes during the summer. As for the remaining models, the traditional approach appears to again be over estimating hmF1 by 5-25km and the NeQuick model, while performing well in the morning and evening, overestimates hmF1 around local noon. Interestingly, we see here that the best fitted solar zenith angle curve underestimates the amplitude of the diurnal variation of hmF1 and performs better during daytime periods than during the evening and morning periods. This is likely because of the abundance of daytime data as compared to morning and evening data (e.g. the fit is heavily weighted toward local noon). The inability of this function to capture the diurnal variation of hmF1, suggests that hmF1 may have a significant dependence on factors that do not simply follow a solar illumination-driven pattern at high latitudes. Finally, and perhaps most interesting, we have the observed behaviour with respect to integrated AE index. Here we note a rapid increase in hmF1 from very quiet periods to more average periods, with largely linear behaviour thereafter. Interestingly, the hmF2-based parameterization of the NeQuick seems to capture the trend with respect to AE index reasonably well, if one ignores the slight tendency for an upward bias. In fact, if one uses 105 km for hmE in place of the NeQuick’s 120 km value, we see average AE index behaviour comparable to that of the E-CHAIM model. This is also true for the latitudinal behaviour of the NeQuick’s parameterization. This suggests that the NeQuick approach to modeling hmF1 is not without merit and that hmF2 may be a good target parameter when attempting to model hmF1. It should be noted, however, that we have here used measured hmF2, and thus the CCIR-based hmF2 of the NeQuick would not capture such geomagnetic variabilities, as it does not include a geomagnetic activity adjustment.

**Table 1** RMS errors from each hmF1 modeling method tested.

Method	RMS Error (km)
Mean	15.01
E-CHAIM	9.47
NeQuick	17.89
NeQuick (hmE = 105km)	15.48
Traditional Model	26.57
SZA Quadratic Fit	14.43

Overall RMS errors from each method are listed in Table 1. One will note from this table that the RMS error of the traditional approach is significantly worse than the use of a constant mean value for hmF1 and that the NeQuick’s use of 120km for hmE also performs worse than a simple mean. In fact, if one used CCIR-derived hmF2 in the NeQuick parameterization, it can be presumed that these errors might have been much larger, given the errors in the IRI/NeQuick hmF2 presented in Themens et al. [2014; 2017]. Overall, the E-CHAIM fit performs substantially better than the mean and the NeQuick. It also performs much better than functions that are based solely on solar zenith angle. While independent validation of these hmF1 and hmE parameterizations may be of interest, we have here used all available hmF1 data for fitting. We will instead opt to validate the entire E-CHAIM bottomside model together rather than validating components of the model individually. This validation is conducted in Section 6.

## 4 The E-CHAIM Bottomside Function

---

Once hmF1 and hmE models have been completed, we proceed to develop a model for the shape of the E-CHAIM bottomside. To define the shape of the bottomside electron density profile within E-CHAIM, we have chosen to create our own, unique, formulation built loosely upon the existing framework of the NeQuick model. In our formulation, we model the bottomside as a single semi-Epstein layer with an altitude-varying scale height.

$$N(h) = \text{sech}^2\left(\frac{h - \text{hmF2}}{H(h)}\right) \#(7)$$

The functions used to define the scale height of the bottomside are themselves taken as a sum of semi-Epstein layers given below.

$$H' = H_{F2} + H_{F1} \left[ \text{sech}^2\left(\frac{h - \text{hmF1}}{0.5(\text{hmF2} - \text{hmF1})}\right) \right] + H_E \left[ \text{sech}^2\left(\frac{h - \text{hmE}}{30.0}\right) \right] \#(8)$$

$$H(h) = H' \cdot \left[ \frac{1}{1 + \exp\left(\frac{\text{hmE} - 15.0 - h}{2.5}\right)} \right] \#(9)$$

where  $H_{F2}$ ,  $H_{F1}$ , and  $H_E$  are amplitude terms,  $H'$  is an intermediate scale height function, and  $H$  is the true scale height used by the model in Equation 7. You will note that the scale height function of Equation 8 is composed of two semi-Epstein layer functions, centered at hmF1 and hmE, with predefined thicknesses. These thicknesses were determined by trial and error. In Equation 9, we arrive at the true modeled scale height, where the scale height function of Equation 8 is multiplied by a sigmoid function. This sigmoid function acts to suppress the scale height below the E-region, ensuring that the electron density tends to zero at the model's lower boundary. Equations 8 and 9 thus require that we model five parameters: hmE, hmF1,  $H_{F2}$ ,  $H_{F1}$ , and  $H_E$ .

While hmE and hmF1 were available from the ionosonde record,  $H_{F2}$ ,  $H_{F1}$ , and  $H_E$  must be fitted from electron density profiles directly. This is done through the use of non-linear least squares, where we make use of the Levenberg-Marquardt method with diagonalized measurement error covariances and pre-specified values for the heights of the scale height layers. Ionosonde inversion errors are used to create a diagonalized measurement error covariance, the a priori covariances are also diagonalized, and all output amplitude values are constrained to be greater than zero. For the E-Region and F1-layer, initial values were selected by inverting Equation 7 and evaluating the resulting function at hmF1 and hmE minus the initial  $H_{F2}$  value. For the  $H_{F2}$  a priori estimate, we use the best fitted  $H$  value from Equation 7, using only data within 30km of the F2 peak. Examples of the fits used to determine  $H_{F2}$ ,  $H_{F1}$ , and  $H_E$  from ionosonde-derived electron density profiles are provided in Figure 6.

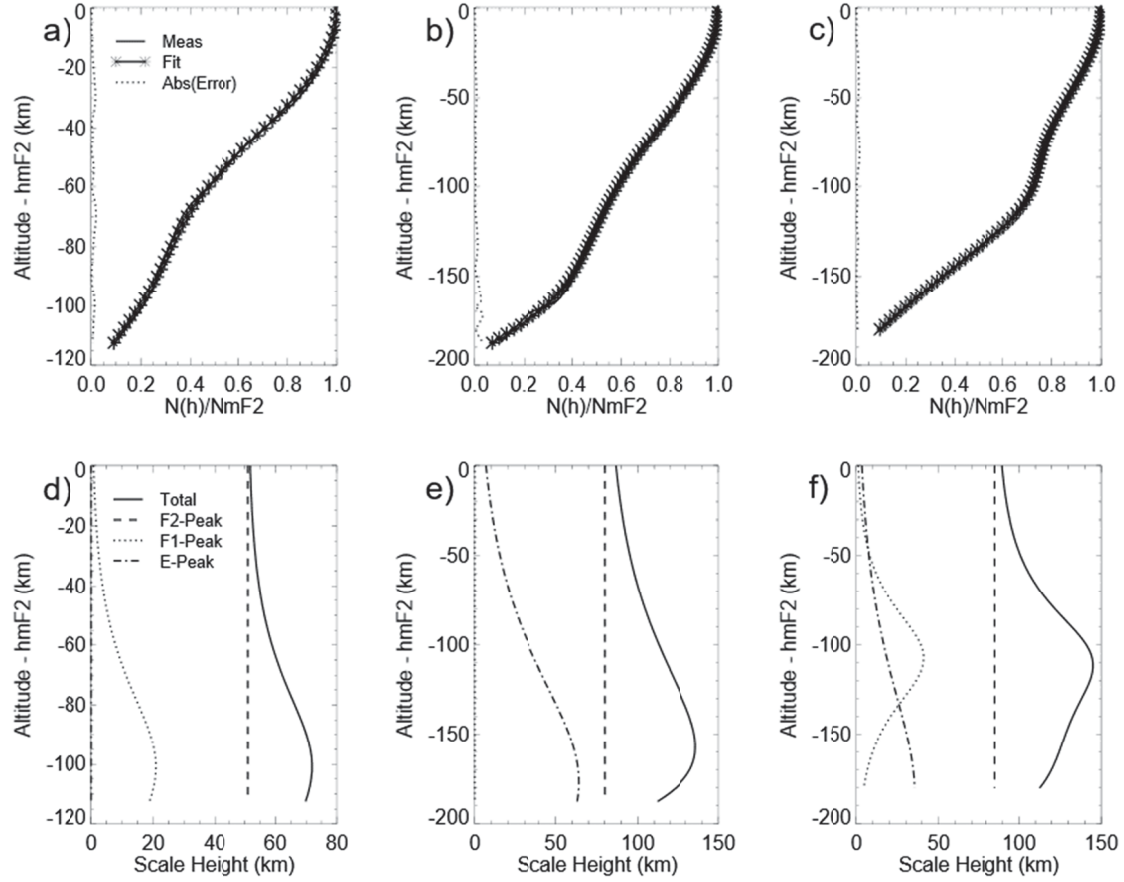


**Figure 6** Example ionosonde-derived electron density profiles at Cambridge Bay (a-c) and corresponding scale height profiles (d-e) for three situations: (a,d) no E-region trace, (b,e) no F1-layer/ledge trace, and (c,f) a profile with all three layers present. (d-f) also demonstrate the various components of the scale height function, where the dotted line is the scale height function for the F1-layer/ledge, the dashed line is the constant term, the dash-dotted is the scale height function for the E-region, and the solid line is the final bottomside scale height function.

As you may note, our chosen profile function does an excellent job fitting ionosonde-derived electron density profiles under a variety of conditions. That said, there are an enormous number of profile functions that will fit an electron density profile. The challenge is finding one that produces physically consistent parameter variability that can be easily fitted to a model. For example, we attempted to use a fourth order polynomial to represent the scale height in our model; however, multiple attractors and the fact that none of the parameters of the fit were tied to a physical phenomenon meant that the fitted parameters did not exhibit coherent variability that could be easily fitted to a model. Our approach, of course, is not without some caveats: the various layers will often overlap, causing unwanted correlations between the layer amplitudes. Nonetheless, through trial and error, we have found that simply fitting for the  $H_E$ ,  $H_{F1}$ , and  $H_{F2}$  parameters of Equation 8 produced satisfactorily coherent and easily modeled parameter variabilities.



An example of the monthly median  $H_{F2}$ ,  $H_{F1}$ , and  $H_E$  behaviour at the Dourbes (4.6°E, 50.1°N) ionosonde is presented in Figure 7. We see in this figure largely expected behaviour: 1)  $H_{F1}$  and  $H_E$  that are strongly correlated with solar zenith angle; 2)  $H_{F2}$  that features solar zenith angle control in the summer with reversed diurnal variability during the winter, which was similarly observed in the B0 bottomside thickness parameter behaviour presented in Themens et al. [2014] for high latitude regions. As you will note, the F1-Layer and E-Region thickness parameters smoothly transition from zero during periods without an F1-Layer or E-region (nighttime periods) to periods with such layers. This ensures that there is a continuous progression between the presence and absence of these layers that should be easily modeled. This, combined with our use of an explicitly continuous profile function, allows us to avoid the concerns with the IRI and NeQuick that are listed in the introduction section of this study.



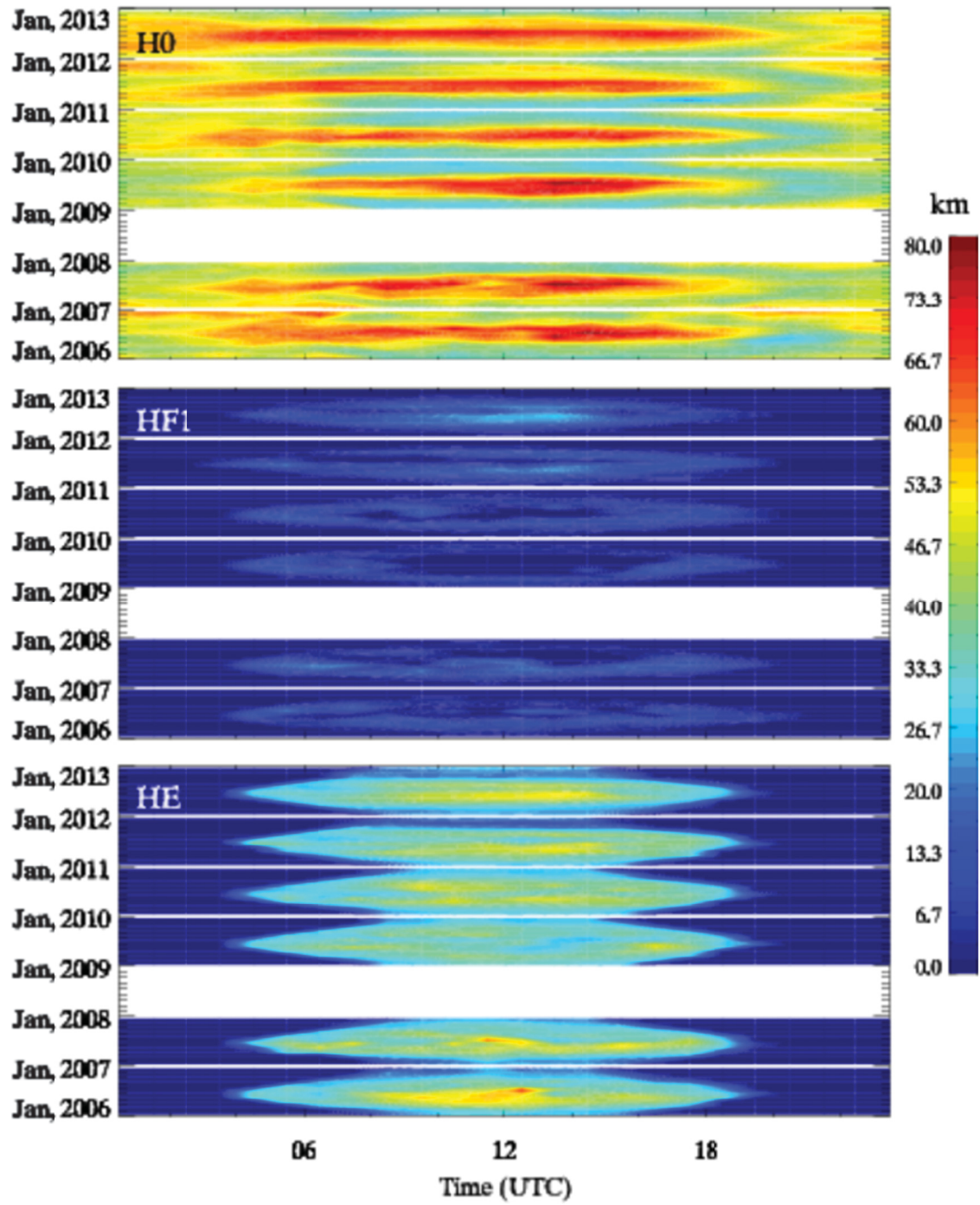


*Figure 7* Contours of monthly median fitted  $H_{F2}$  (top),  $H_{F1}$  (middle), and  $H_E$  (bottom) for the Dourbes ionosonde between 2006 and 2013.

## 5 Parameterization of the Bottomside Scale Height Amplitudes

---

To parameterize the bottomside scale height amplitudes ( $H_E$ ,  $H_{F1}$ , and  $H_{F2}$ ), we use the same methodology as that used for each of the other model components; namely, we have chosen to use three identical spherical cap harmonic expansions with Fourier expansions in day of year as Gauss coefficients. These parameterizations are functionally identical to that used for hmF1 (e.g. Equations 1 – 4) but with a degree and order of  $L = 5$  and  $M = 5$ . The choice to use identical parameterizations here was largely made for computational purposes to remove the need to build a new parameter basis set for each component of the bottomside model.

## 6 Validation

---

To validate the performance of the E-CHAIM bottomside model, we have gathered data from a selection of Incoherent Scatter Radars (ISRs), which were not included in the fitting dataset, and compared model errors with respect to those found using IRI 2016. Since the AMTB-2013 bottomside thickness model was not designed for use above  $60^\circ\text{N}$  geomagnetic latitude, we will here use the Gulyaeva B0 model option of Gulyaeva [1987], which slightly outperforms the IRI Table option at high latitudes [Themens et al. 2014]. The processing of the ISR dataset is done in the same manner as that detailed in Themens et al. [2018]. For the purpose of only examining the performance of the bottomside shape functions and parameterization, we have used measured hmF2 and NmF2 as inputs to E-CHAIM and the IRI in the following analysis. Also, to diminish the impact of the F2 peak, we have further normalized all of the resulting electron density profiles to NmF2 and hmF2. Figure 8 presents an example of the resulting normalized, peak-relative electron density profiles from the Poker Flat ISR (PFISR). Data gaps in the following figures that are not consistent across time of day in (e.g. white spaces that are only not in all four UTC time plots) may be mostly attributed to the inability to define an F2-peak (and thereby NmF2 and hmF2) from the data at those times. This is most common at night, either when strong precipitation in the E-region or lower F-region makes defining an F2-peak ambiguous or when the F2 peak is characterized by high hmF2 and low density, resulting in the peak being indistinguishable from the increasingly more significant background noise in ISR data at high altitudes. Other white areas correspond to altitudes that do not have data, which are largely dependent on hmF2.

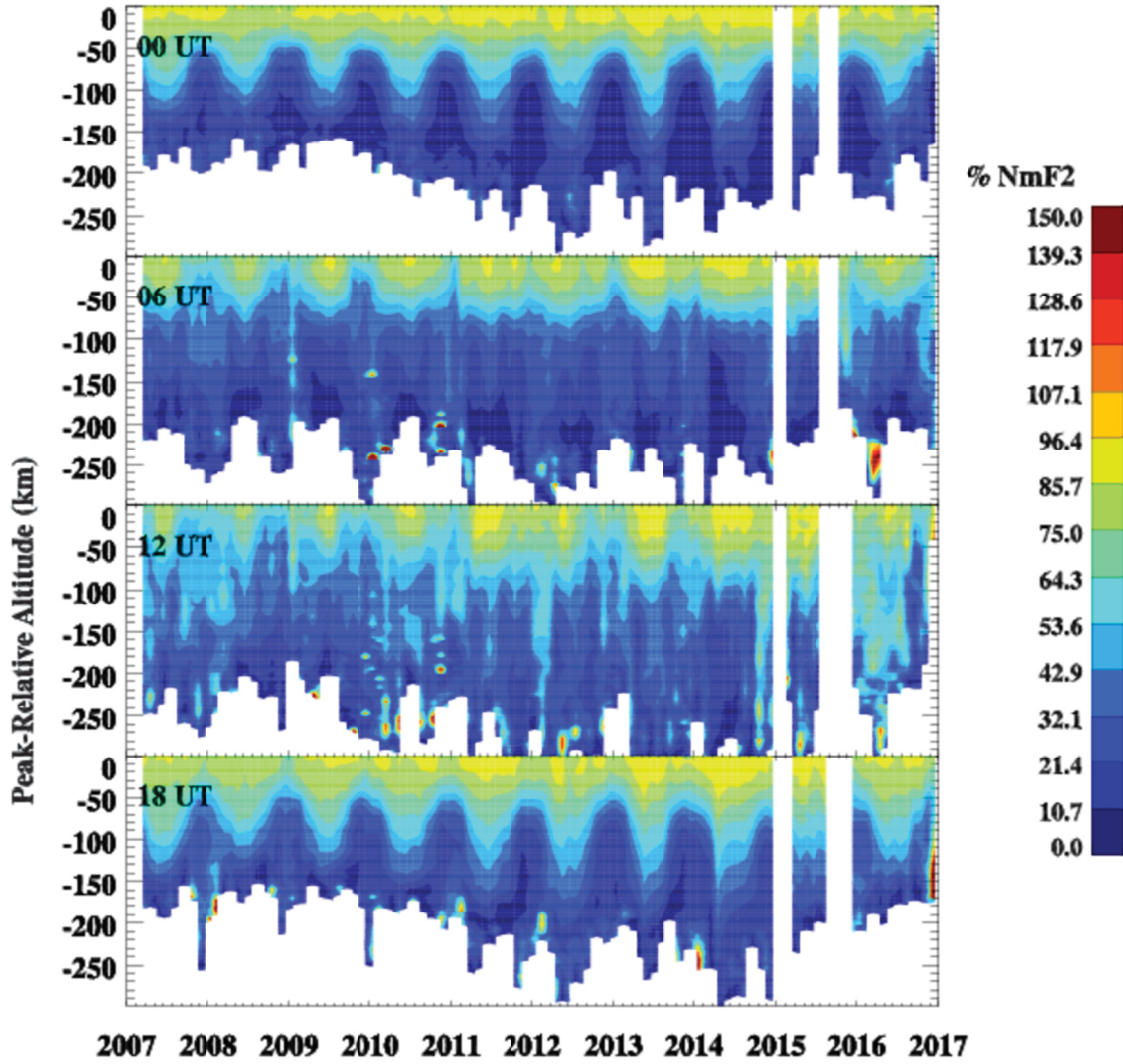


**Figure 8** F2-peak normalized monthly median electron density profiles at PFISR for various UT times between 2007 and 2015. Note that local time at Poker Flat is UT – 8.1 hours.

In Figure 8, one will note many standard, expected bottomside variabilities: 1) enhanced F1-Layer and E-Region densities during summer and daytime periods, 2) the absence of an F1-Layer at night, 3) an F-region that exhibits reduced thickness variability seasonally and with solar activity during nighttime conditions, and 4) a strong seasonal and solar cycle variation in F-region thickness during daytime periods, where F-region thicknesses are largest during the summer and at high solar activity.

In Figure 9 we present the differences between model and measured bottomside peak-relative density for the same PFISR dataset at four UT times (note Poker Flat local time is UT – 8.1 hours).

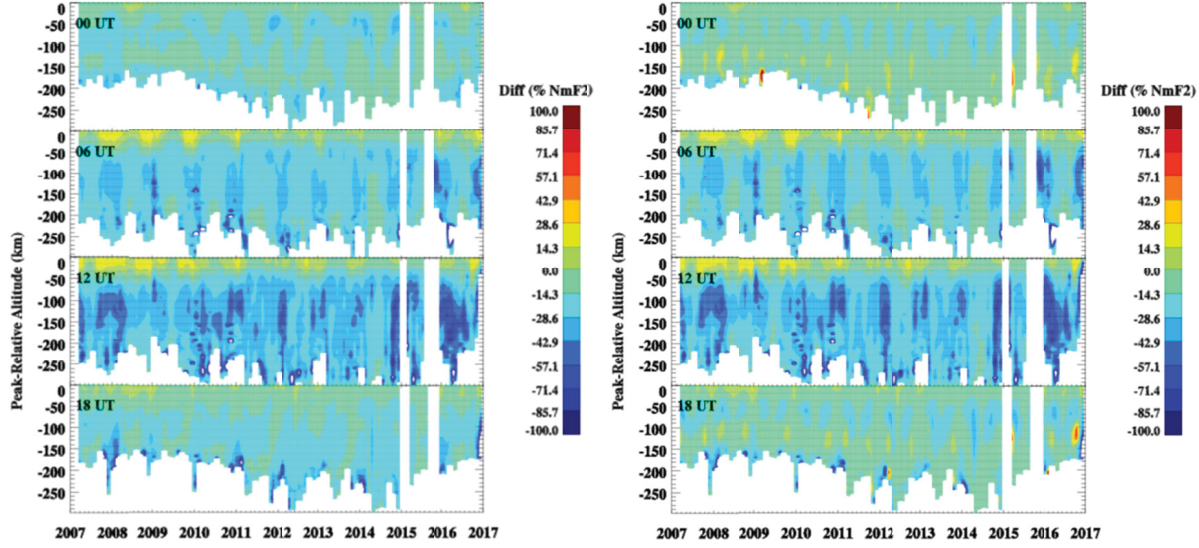


**Figure 9** Model-to-measurement bottomside monthly median electron density errors for E-CHAIM (left) and the IRI (right) at PFISR between 2007 and 2015.

From this figure, we see that both bottomside models demonstrate a very similar tendency toward underestimation of the peak-normalized bottomside electron density at PFISR, particularly during winter nighttime conditions. The similarity between the nighttime errors will be discussed in more detail in Section 7. During daytime conditions, errors from both models appear mostly constrained to the lower F-Region. For E-CHAIM, this is indicative of an underestimation of the  $H_{F2}$  or  $H_{F1}$  scale amplitude during these periods or an inability of the model function to capture the curvature of the near-peak electron density profile [Themens et al., 2017b]; however, the similar error patterns exhibited by the IRI, which uses a vastly different profile shape function, suggests that the latter is unlikely. To better visualize the comparison of the performance between the E-CHAIM and the IRI we have plotted contours of the differences between IRI and E-CHAIM RMS errors at PFISR in Figure 10. In this figure, negative values correspond to periods where E-CHAIM outperforms the IRI and vice versa.



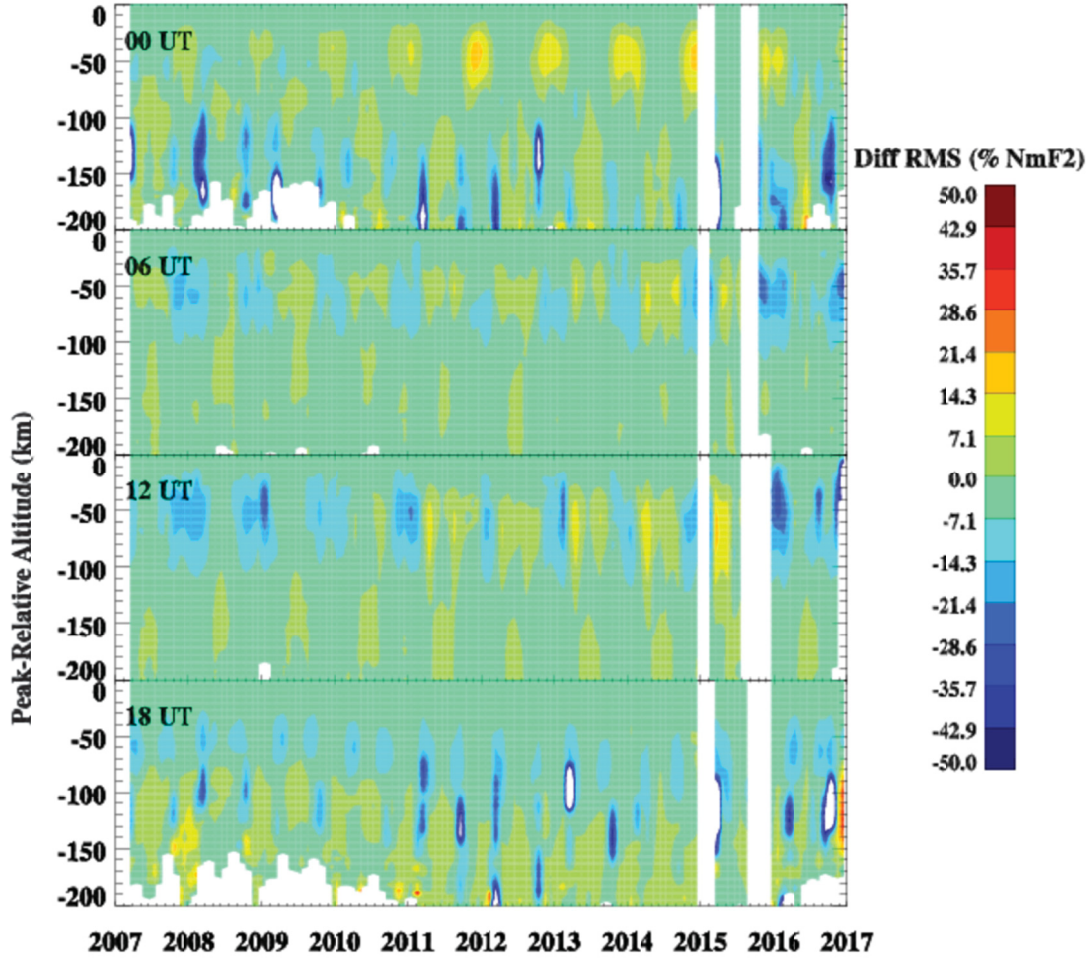


**Figure 10** Differences between IRI and E-CHAIM bottomside electron density profile RMS errors at PFISR. Negative values correspond to periods and locations where E-CHAIM outperforms the IRI.

From this figure, it is much easier to see that the IRI outperforms the E-CHAIM bottomside shape model in the F-region during early evening periods (00UT) at this location, with the exception of the E-region. The increased IRI error in the E-region during these periods is largely due to IRI's Auroral E-region model [Zhang and Paxton, 2008], which has been turned on for this study. This Auroral E-Region model is found through these comparisons to ISR data to overpredict precipitation-induced enhancement in equinox E-region densities. At night time, E-CHAIM outperforms the IRI at F-Region altitudes during the winter and equinoxes, particularly at low solar activity. During equinox morning periods (18UT), E-CHAIM demonstrates a significant improvement over the IRI of over 50% of NmF2 but is outperformed by the IRI in the E-Region by up to 10% of NmF2. Both models demonstrate comparable performance during other periods. Similar to Figure 10, we may also examine these performance differences at the EISCAT Svalbard ISR and the north face of the Resolute ISR (RISR-N) in Figure 11.

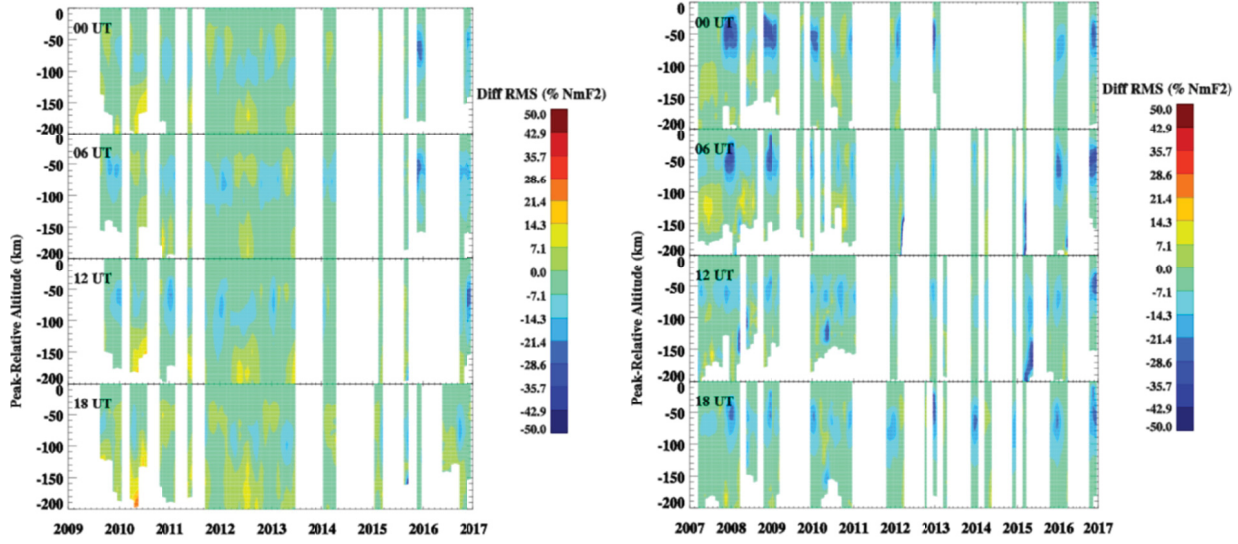


**Figure 11** Same as Figure 10 but for RISR (left) and the Svalbard ISR (right).

For the Svalbard ISR, we see significantly better performance from E-CHAIM over the IRI in the F-region for all periods of the day and particularly during winter periods where improvement reached over 40% of NmF2. E-CHAIM does, however, perform slightly worse than the IRI in the E-region during early-morning and nighttime periods at low solar activity, with comparable performance elsewhere. At RISR, we see improved performance from E-CHAIM in the F-region during nighttime periods and during winter daytime periods, but reduced performance compared to the IRI in the E-region during summer daytime.

For a better impression of the overall performance of the E-CHAIM and IRI bottomside models, we present plots of the bottomside electron content (integral of the electron density up to hmF2) in Figure 12. Keep in mind when evaluating this figure that it was generated using measured NmF2 and hmF2; thus, the bottomside electron content differences are only indicative of integrated differences in the bottomside shape and not of the true bottomside electron content.

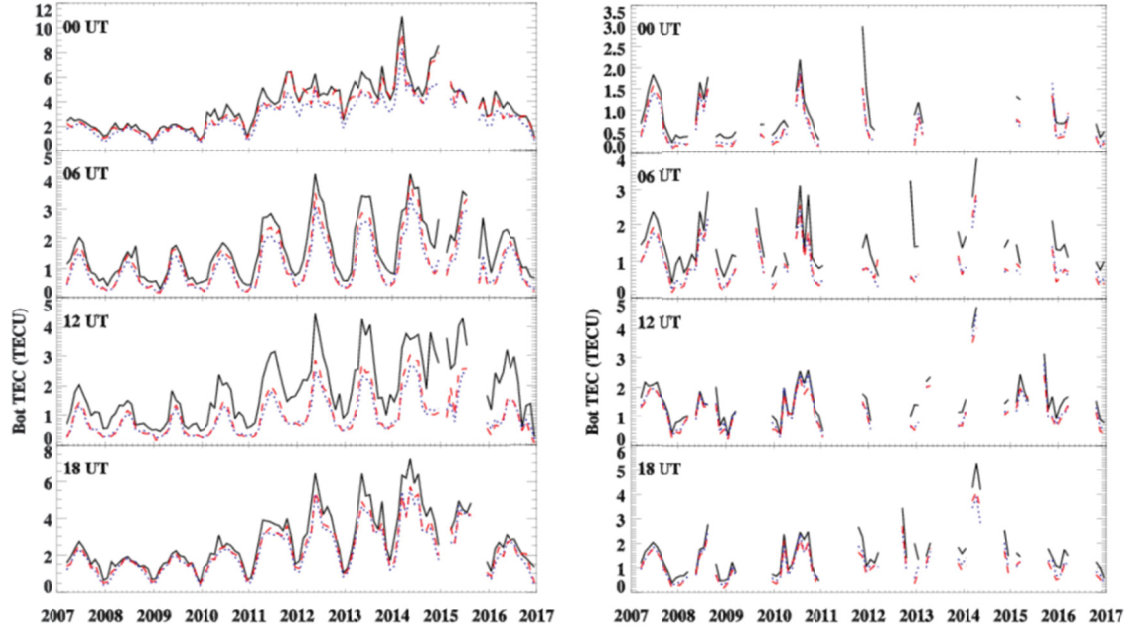


**Figure 12** Bottomside electron content measured by the PFISR (left) and Svalbard (right) ISRs and that modeled by the IRI (red) and E-CHAIM (blue) between 2007 and 2015 at various UT times. Note that the Poker Flat local time is UT – 8.1 and that for Svalbard is UT + 1.4.

In this figure, we see that both models perform reasonably well in their overall representation of the bottomside electron density when NmF2 and hmF2 are accurate. Errors in bottomside electron content, under these circumstances, did not exceed 1.6 TECU ( $10^{16}$  e/m<sup>3</sup>); however, we still note a tendency for both models to underestimate electron density during nighttime periods.

Overall, despite improvements over the IRI during winter and nighttime periods, E-CHAIM demonstrates a tendency to underestimate the thickness of the F-layer during summer daytime periods and, partially by extension, the density in the E-region. This issue could be attributed, at least in part, to the noisy nature of ionosonde-based electron density profile scale heights. Even in manually scaled datasets, noise in F2-peak scale heights can exceed 15km. Ultimately, E-CHAIM's bottomside performs comparably to that of the IRI; however, future work should explore methods of improving these shortcomings. To that end, we will explore the possibility of modeling the bottomside entirely within the electron density domain and examine further refining data quality control measures in future versions of the model.



## 7 Comment Regarding Night Time Underestimation

One may note from Figure 9 that errors as a percentage of NmF2 are particularly large during nighttime periods at altitudes further than 50km from the F2-peak, where errors are as large as 65% of NmF2. One will note that there is a high degree of commonality between the errors in the IRI and E-CHAIM during night time periods, leading the author to suspect that these errors are not a result of the model functions chosen. These high errors with respect to NmF2 likely come about through two main mechanisms:

- 1) NmF2 is quite low during winter night time periods, so even small errors in bottomside electron density will be presented as large errors with respect to NmF2.
- 2) Both of these models were developed using solely ionosonde data; however, ionosonde data suffers the limitation that there exists a lower threshold, below which they are incapable of providing information ( $\sim 1.0 - 2.0$  MHz depending on absorption conditions). This means that ionosondes are intrinsically incapable of observing small, but not non-negligible, densities that occur during winter nighttime periods. An example of this issue during a nighttime period at Millstone Hill is presented in Figure 13.

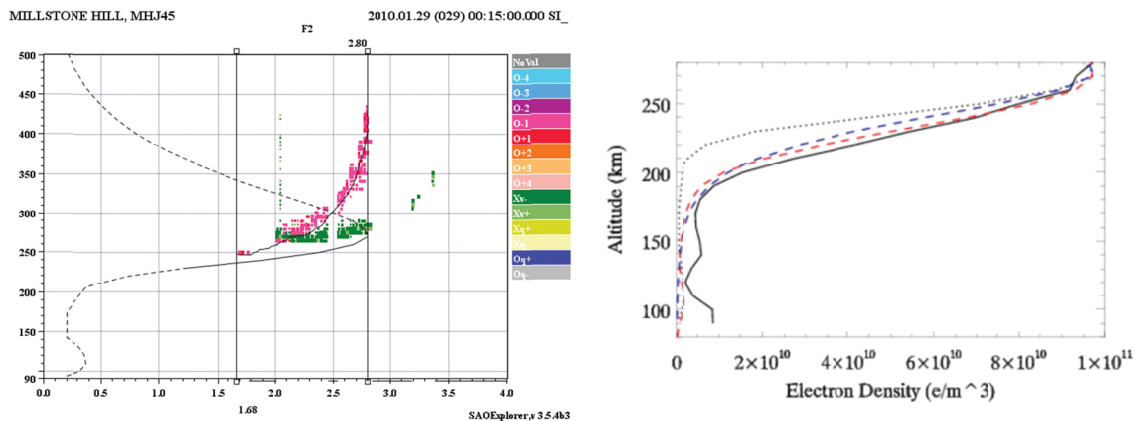


**Figure 13** Left: A manually scaled ionogram from the Millstone Hill Digisonde at 00:15 UT on January 29<sup>th</sup>, 2010. Right: Corresponding vertical electron density profiles from the Millstone Hill ISR (solid black), the Millstone Hill ionosonde (dotted black), E-CHAIM anchored at the ionosonde hmF2 and NmF2 (dashed blue), and the IRI anchored at the ionosonde hmF2 and NmF2 (red dashed) at 00:15 UT on January 29<sup>th</sup>, 2010

In the above figure, we note that there is a significant discrepancy between the manually scaled ionosonde profile and the Millstone ISR profile. Because of the very low densities during this period, the E-region trace (which should exist with a peak at  $\sim 0.9$  MHz, given the ISR profile) is well below the minimum observable frequency of the ionosonde and is thus not represented in the ionogram. Also, no E-F-valley retardation cusp is observed in the ionogram, as this would have

likely occurred below the minimum observable frequency of the ionosonde. The lack of this cusp and the E-region trace affects the inversion's ability to reconstruct the thickness of the bottomside and leads to underestimation. In addition to this, ionosondes are incapable of resolving the depth of the E-F-valley, the density of which may be underestimated by the current ionosonde dataset.

These concerns suggest that future versions of these models may be well served through the use of a different dataset, such as ISR data.

## 8 Challenges due to Precipitation

Despite the comparable performance between the IRI and E-CHAIM bottomside parameterizations, both models demonstrate a marked shortcoming in their ability to represent the bottomside electron density profile during periods of strong precipitation. For example, we have plotted electron density profiles from Poker Flat ISR (PFISR) in Figure 14, which demonstrate reasonable performance by both models during periods not subject to significant precipitation and demonstrate comparably poor performance during periods of enhanced precipitation. In these examples, we have ingested measured hmF2 and NmF2 into the models, such that we are only comparing the profile shape in the absence of errors in hmF2 and NmF2. We have also left the IRI auroral precipitation model turned on.

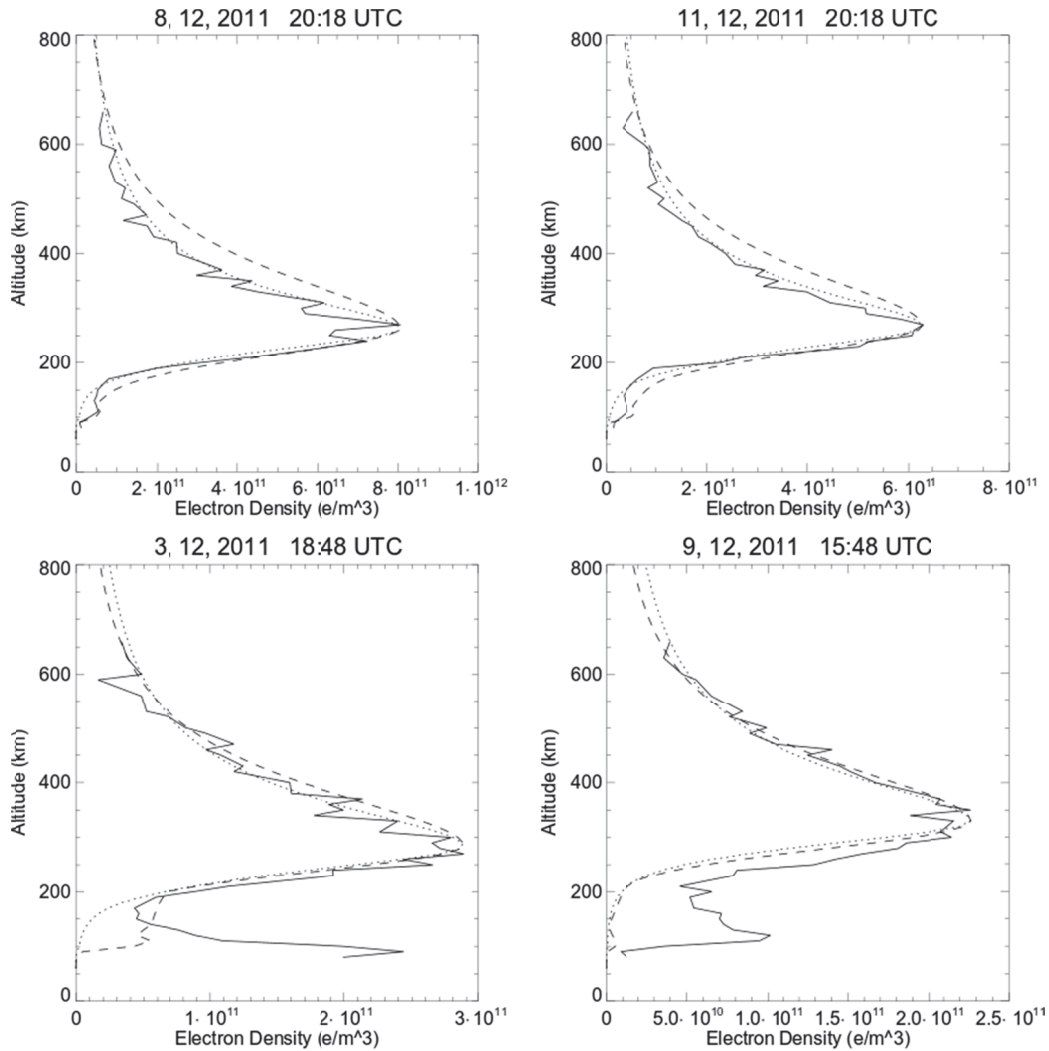


**Figure 14** Example electron density profiles from PFISR without (top) and with (bottom) auroral precipitation structures. Solid lines correspond to measured profiles, dotted lines correspond to

*E-CHAIM, and dashed lines correspond to the IRI. Note that ISR hmF2 and NmF2 have been used here in place of the model values to facilitate comparison of just the profile shape. Profile dates (day, month, year UTC) are provided in the title of each subplot.*

We note that the IRI E-region, in the absence of strong precipitation, performs quite well at all locations in this study, aside from a slight tendency toward overestimation at nighttime; however, one should note that, during periods of precipitation, the IRI's auroral precipitation model sees its improvement over the climatology countered by worse performance during "false alarm" situations (i.e. situations where the IRI predicts auroral precipitation but none is present). This trigger issue will be an important consideration in the adoption of such a precipitation model in E-CHAIM.

Particularly challenging in these situations is the fact that ionosondes are incapable of providing electron density profiles under strong precipitation conditions, where E-region densities are greater than those of the F-Region, and cannot provide information about the highly variable state of the E-F valley during precipitation conditions. This severely limits the datasets that can be used to model the bottomside under these conditions. In this way, the datasets that were used for fitting the bottomside in the IRI and E-CHAIM are biased against these conditions and, by construction, cannot represent these features; thus, an approach like that of Zhang and Paxton [2008] is an attractive option.

## 9 Conclusion

---

We have here presented the bottomside electron density model function used by E-CHAIM. Through the development of this bottomside function, we have been able to provide comparable performance to the bottomside shape of the IRI while avoiding standard practices that demonstrate discontinuities in time and space.

In the process of developing the E-CHAIM bottomside function, we have found that the “traditional” ICEPAC hmF1 function performs very poorly with RMS errors greater than 25km compared to a standard deviation about the mean of only ~15km. In terms of hmE, we find that the IRI’s use of 105km is accurate for our dataset, while the NeQuick’s use of 120km is several standard deviations larger than the measured mean. Also, while the NeQuick hmF1 estimation method demonstrates comparable overall behaviour to that seen in the measured dataset, it is biased toward overestimation by 5-15km. The use of the IRI’s  $hmE = 105km$  instead of the NeQuick value results improved performance with RMS errors of 15.48km instead of the NeQuick’s original 17.89km RMS errors. This, however, remains above the standard deviation about the measured mean (15.01km).

In terms of overall bottomside performance, the E-CHAIM bottomside is demonstrated to outperform the IRI bottomside function in the F-region during low solar activity periods. At high latitudes, E-CHAIM tends to outperform the IRI during winter months by between 10% and 40% of NmF2 while being outperformed by the IRI by between 10% and 25% of NmF2 during summer periods, particularly during the daytime at high solar activity. In general, E-CHAIM’s errors tend toward underestimation of bottomside electron density. In general, we also find that the IRI performs well at all locations in the E-region during daytime conditions but suffers errors due to the over prediction of auroral precipitation enhanced E-region density, particularly during the equinoxes. Both models suffer poor performance during precipitation events, particularly in the auroral oval. Future work will examine the use of ISR data for the model fitting and explore the application of a precipitation model in the E-CHAIM bottomside parameterization.

## References/Bibliography

---

- Altadill, D., J.M. Torta, and E. Blanch (2009), Proposal of new models of the bottom-side B0 and B1 parameters for IRI. *Adv. Space Res.*, 43, 1825-1834, doi:10.1016/j.asr.2008.08.014
- Altadill, D., S. Magdaleno, J.M. Torta, and E. Blanch (2013), Global empirical models of the density peak height and of the equivalent scale height for quiet conditions, *Adv. Space Res.*, 52, 1756-1769, doi:10.1016/j.asr.2012.11.018
- Bilitza, D. (1990), International Reference Ionosphere 1990, NSSDC 90-22, Greenbelt, Maryland.
- Bilitza, D. (2003). International Reference Ionosphere 2000: Examples of improvements and new features. *Adv. Space Res.*, 31(3), pp. 757-767.
- Gulyaeva, T. L. (1987), Progress in ionospheric informatics based on electron density profile analysis of ionograms, *Adv. Space Res.*, 7(6), 39-48.
- Jayachandran, P. T., R. B. Langley, J. W. MacDougall, S. C. Mushini, D. Pokhotelov, A. M. Hamza, I. R. Mann, D. K. Milling, Z. C. Kale, R. Chadwick, T. Kelly, D. W. Danskin, and C. S. Carrano (2009), Canadian High Arctic Ionospheric Network (CHAIN), *Radio Sci.*, 44, RS0A03, doi:10.1029/2008RS004046.
- Kelso, J.M. (1968), Ray Tracing in the Ionosphere, *Radio Sci.*, 3(1), doi: 10.1002/rds1968311
- Nava, B., P. Coïsson, and S.M. Radicella (2008), A new version of the NeQuick ionosphere electron density model. *J. Atmos. and Solar-Terr. Phys.*, 70(15), 1856-1862 doi:10.1016/j.jastp.2008.01.015
- Reinisch, B., and X. Huang (2000), Redefining the IRI F1 Layer profile, *Adv. Space Res.*, 25(1), 81-88.
- Reinisch, B. W., and I. A. Galkin (2011), Global ionospheric radio observatory (GIRO), *Earth, Planets, and Space*, 63, 377-381, doi:10.5047/eps.2011.03.001
- Stewart, F. G. (1988), Ionospheric Communications Enhanced Profile Analysis & Circuit (ICEPAC) Prediction Program Technical Manual. <http://www.voacap.com>.
- Themens, D. R., P. T. Jayachandran, M. J. Nicolls, and J. W. MacDougall (2014), A top to bottom evaluation of IRI 2007 within the polar cap, *J. Geophys. Res. Space Physics*, 119, 6689-6703, doi:10.1002/2014JA020052.
- Themens, D.R., P.T. Jayachandran, I. Galkin, and C. Hall (2017a). The Empirical Canadian High Arctic Ionospheric Model (E-CHAIM): NmF2 and hmF2, *J. Geophys. Res. Space Physics*, doi: 10.1002/2017JA024398
- Themens, D.R., P.T. Jayachandran, and R.H. Varney (2017b), Examining the use of the NeQuick bottomside and topside parameterizations at high latitudes, *Adv. Space Res.*, 68(1), doi:10.1016/j.asr.2017.09.037
- Themens, D.R., et al. (2018), Topside Electron Density Representations for Middle and High Latitudes: A Topside Parameterization for E-CHAIM Based on the NeQuick, *Journal of Geophysical Research: Space Physics*, 123, 2, 1603-1617.

Zhang, Y., and L.J. Paxton (2008), An empirical Kp-dependent global auroral model based on TIMED/GUVI FUV data. *J. Atmos. Solar Terr. Phys.*, 70, 1231-1242, doi:10.1016/j.jastp.2008.03.008.

This page intentionally left blank.



## List of symbols/abbreviations/acronyms/initialisms

---

DND	Department of National Defence
E-CHAIM	Empirical Canadian High Arctic Ionospheric Model
IRI	International Reference Ionosphere
NmF2	Peak density of the F2-layer
hmF2	Height of the F2-layer peak
foF2	The F2-layer critical frequency
M3000F2	Ratio of the MUF to foF2
MUF(3000)	Maximum Usable Frequency at 3000km distance
CHAIN	Canadian High Arctic Ionospheric Network
IRTAM	IRI-based Real-Time Assimilative Model
GIRO	Global Ionospheric Radio Observatory
MIT	Main Ionospheric Trough
DRDC	Defence Research and Development Canada
DSTKIM	Director Science and Technology Knowledge and Information Management

DOCUMENT CONTROL DATA		
*Security markings for the title, authors, abstract and keywords must be entered when the document is sensitive		
1. ORIGINATOR (Name and address of the organization preparing the document. A DRDC Centre sponsoring a contractor's report, or tasking agency, is entered in Section 8.) <b>University of New Brunswick</b> <b>8 Bailey Drive</b> <b>P.O. Box 4400</b> <b>Fredericton (New Brunswick) E3B 5A3</b>		2a. SECURITY MARKING (Overall security marking of the document including special supplemental markings if applicable.) <b>CAN UNCLASSIFIED</b>
		2b. CONTROLLED GOODS <b>NON-CONTROLLED GOODS</b> <b>DMC A</b>
3. TITLE (The document title and sub-title as indicated on the title page.) <b>The Empirical Canadian High Arctic Ionospheric Model (E-CHAIM): Bottomside</b>		
4. AUTHORS (Last name, followed by initials – ranks, titles, etc., not to be used) <b>Themens, D.; Jayachandran, P.T.; McCaffrey, A.; Reid, B.</b>		
5. DATE OF PUBLICATION (Month and year of publication of document.)  <b>October 2018</b>	6a. NO. OF PAGES (Total pages, including Annexes, excluding DCD, covering and verso pages.)  <b>29</b>	6b. NO. OF REFS (Total references cited.)  <b>16</b>
7. DOCUMENT CATEGORY (e.g., Scientific Report, Contract Report, Scientific Letter.) <b>Contract Report</b>		
8. SPONSORING CENTRE (The name and address of the department project office or laboratory sponsoring the research and development.)  <b>Corporate Office</b> <b>ADM(S&amp;T) / DRDC Corporate</b> <b>NDHQ (Carling), 60 Moodie Drive, Building 7</b> <b>Ottawa, Ontario K1A 0K2</b> <b>Canada</b>		
9a. PROJECT OR GRANT NO. (If appropriate, the applicable research and development project or grant number under which the document was written. Please specify whether project or grant.)  <b>03ba - Air Integrated – RF</b>	9b. CONTRACT NO. (If appropriate, the applicable number under which the document was written.)  <b>W7714-186507/001/SS</b>	
10a. DRDC PUBLICATION NUMBER (The official document number by which the document is identified by the originating activity. This number must be unique to this document.)  <b>DRDC-RDDC-2018-C184</b>	10b. OTHER DOCUMENT NO(s). (Any other numbers which may be assigned this document either by the originator or by the sponsor.)	
11a. FUTURE DISTRIBUTION WITHIN CANADA (Approval for further dissemination of the document. Security classification must also be considered.)  <b>Public release</b>		
11b. FUTURE DISTRIBUTION OUTSIDE CANADA (Approval for further dissemination of the document. Security classification must also be considered.)		

12. KEYWORDS, DESCRIPTORS or IDENTIFIERS (Use semi-colon as a delimiter.)

Canadian High Arctic Ionospheric Model; International Reference Ionosphere; Ionosphere; Oblique ionospheric sounder; High-frequency Radar.

13. ABSTRACT/RÉSUMÉ (When available in the document, the French version of the abstract must be included here.)

In this study, we present a bottomside model representation to be used by the Empirical Canadian High Arctic Ionospheric Model (E-CHAIM). This model features a new approach to modeling the bottomside electron density; namely, instead of modelling electron density directly, E-CHAIM models the altitude profile of the scale thickness of a single bottomside layer. In this approach the curvature in the bottomside associated with the E-region and F1-layer is represented in the scale thickness domain as a peak function centered at the layer peak altitude. The use of this approach ensures the production of explicitly doubly differentiable bottomside electron density profiles and directly avoids issues known to exist within current standard, such as the International Reference Ionosphere (IRI), which has discontinuities in space, time, and in the vertical electron density gradient. In terms of performance, after removing the impacts of hmF2 and NmF2, the new ECHAIM profile function generally performs comparably to the IRI, with bottomside TEC within 1.6 TECU of observations. More specifically, the E-CHAIM bottomside is demonstrated to outperform the IRI bottomside function in the F-region during low solar activity periods. At high latitudes, E-CHAIM tends to outperform the IRI during winter months by between 10% and 40% of NmF2 while being outperformed by the IRI by between 10% and 25% of NmF2 during summer periods, particularly during the daytime at high solar activity.

Dans cet article, nous décrivons la représentation du modèle du «bas» utilisée par le Modèle empirique de l'ionosphère du haut arctique canadien (E-CHAIM). Ce modèle comporte une nouvelle méthode de modéliser la densité électronique au bas de l'ionosphère. E-CHAIM modélise le profil d'altitude de l'épaisseur de l'échelle d'une unique couche inférieure plutôt que de modéliser directement la densité d'électrons. Avec cette méthode, la courbure du bas associée à la région E et la région F1 est représentée dans le domaine de l'épaisseur de l'échelle comme une fonction de maximum centrée à l'altitude maximale de la couche. Cette démarche assure la production de profils deux fois dérivables de la densité d'électrons au bas de la couche et évite directement les problèmes connus des modèles standards actuels, comme l'ionosphère Internationale de Référence (IIR), qui présente des discontinuités dans l'espace, le temps et le gradient vertical de densité d'électrons. Au chapitre du rendement, après avoir retiré les effets de la hmF2 et de la NmF2, la nouvelle fonction de profil du modèle E-CHAIM se comporte de manière comparable à l'IIR, en prédisant une Teneur Totale en Électrons (TEC) au bas, en deçà de 1,6 unité de TEC des valeurs observées. Plus particulièrement, nous avons montré que la fonction du fond du modèle E-CHAIM surpasse la fonction de fond de la région F pendant les périodes de faible activité solaire. Aux hautes latitudes, E-CHAIM tend à surpasser l'IIR pendant l'hiver par environ 10% à 40% pour la NmF2 alors que l'IIR surpasse E-CHAIM par environ 10 à 25% pour la NmF2 pendant l'été, notamment durant le jour pendant les périodes de forte activité solaire.